crystals

MDPI

Article

Compressive Mechanics and Hyperelasticity of Ni-Ti Lattice Structures Fabricated by Selective Laser Melting

Cong Zhang [1,2], Jiulu Jin [1,2], Meng He [3,4] and Lei Yang [1,2,*]

[1] School of Transportation and Logistics Engineering, Wuhan University of Technology, Wuhan 430063, China; zhangcong@whut.edu.cn (C.Z.); jinjiulu@whut.edu.cn (J.J.)
[2] Hubei Longzhong Laboratory, Xiangyang 441136, China
[3] Gemmological Institute, China University of Geosciences, Wuhan 430074, China; hemoe@cug.edu.cn
[4] School of Civil Environmental Engineering & Architecture, Hubei University of Technology, Wuhan 430068, China
* Correspondence: lei.yang@whut.edu.cn

Abstract: Additively manufactured Ni-Ti lattice structures have controllable bio/mechanical properties, as well as excellent large deformation and damping properties similar to those of natural bone. They have broad application prospects in the field of bone implantation. Triply Periodic Minimal Surface (TPMS) structures are believed to be the most potential and ideal bionic bone structures. In this work, Ni-Ti Gyroid-type TPMS lattice structures were fabricated by selective laser melting (SLM) and their manufacturing fidelity and compression properties were evaluated. By changing the maximum strain value, the hyperelastic recovery performance under cyclic stress was investigated. The results showed that the Ni-Ti Gyroid lattice structures fabricated by SLM had excellent manufacturability (relative density can reach 98.93%) and mechanical properties (elastic modulus is about 130.8 MPa, ultimate strength is about 2.7 MPa). The hyperelastic cycle testing showed that the elastic modulus, yield strength and ultimate strength of the lattice structures tended to stablilize gradually with increasing numbers of cycles. The residual strain increased with the number of cycles, and as the maximum strain increased from 4% to 8%, the residual strain also increased from 1% to 4%.

Keywords: selective laser melting; lattice structure; triply periodic minimal surface; mechanical properties; hyperelasticity

Citation: Zhang, C.; Jin, J.; He, M.; Yang, L. Compressive Mechanics and Hyperelasticity of Ni-Ti Lattice Structures Fabricated by Selective Laser Melting. *Crystals* **2022**, *12*, 408. https://doi.org/10.3390/cryst12030408

Academic Editors: Ludmila Isaenko and Witold Łojkowski

Received: 17 February 2022
Accepted: 15 March 2022
Published: 17 March 2022

1. Introduction

Nickel-titanium (Ni-Ti) alloy is an attractive biomaterial for bone replacement with good biocompatibility, corrosion and wear resistance, high fatigue resistance and unique hyperelasticity [1–4]. The hyperelasticity of Ni-Ti makes it more suitable than conventional metal biomaterials, such as titanium and its alloys, cobalt-chromium alloys, and stainless steel, for scenarios that need to carry cyclic forces.

For many years, the production of Ni-Ti porous structures has been dominated by traditional fabrication techniques such as powder metallurgy [5,6], high temperature synthetic hot static pressing [7] and metal injection molding [8]. The Ni-Ti porous structures prepared by these methods usually have random pore distribution and low dimensional accuracy, resulting in poor controllability and repeatability of the mechanical and biological properties of the structures. On the other hand, application requirements often require materials with individual profiles and layered internal structures. This places high demands on the design and fabrication of lattice structures, which are difficult to meet by the above-mentioned traditional methods [9]. In recent years, additive manufacturing (AM) technologies such as Selective Laser Melting (SLM) have developed rapidly, and have greatly facilitated the highly flexible design and high-precision fabrication of porous materials [10–14]. AM not only enables the fabrication of microstructured dense and fine Ni-Ti lattice structures, but also allows easy tuning and precise control of pore geometry to

tailor performance, perfectly adapting to the special fabrication needs of high-quality and customized Ni-Ti [15–18].

Lattice structures, which are topologically ordered porous structures based on one or more repeating unit cells, have been the most popular porous structures for additive manufacturing due to their simplicity in design, modeling, and geometric tuning [19]. At present, Ni-Ti lattice structures mainly adopt pillar-based lattice structures composed of multiple cylindrical or cuboid pillars, such as simple cubic (SC) [20–22], body-centered cubic (BCC) [23–25] and octahedral structures [26,27]. However, the geometric transition at the joints of the support rods in a lattice-based structure is abrupt and non-uniform, making it prone to severe stress concentration under load, leading to early fracture near the joints [28,29]. Furthermore, due to the lack of supports, pillar-based lattice structures typically exhibit poor manufacturability and geometric fidelity during additive manufacturing [30].

Triply Periodic Minimal Surface (TPMS) lattice structures have a smooth outer surface, as well as a continuous and uniform radius of curvature, thus exhibiting more uniform stress distribution and better mechanical properties under loading, compared with conventional pillar-based lattice structures [31,32]. To achieve customized design and fabrication of lattice structures with Ni-Ti TPMS, it is necessary to systematically understand the relationship between lattice unit cell geometry and its manufacturability and mechanical properties. Some studies have been reported on the effects of lattice unit cell types on the structural properties of Ni-Ti TPMS lattices [33]. Speirs et al. [33] compared the fatigue properties of octahedron-type and gyroid-type Ni-Ti lattice structures fabricated by SLM with the same volume fraction of 20%. The results showed that the Gyroid-type TPMS lattice structure showed better fatigue resistance than the octahedral-type structure. However, the effects of maximum strain value on the hyperelastic properties of Ni-Ti TPMS lattice structures have rarely been reported.

Therefore, in this paper, Ni-Ti Gyroid TPMS lattice structures were prepared by SLM, and their surface topography, geometric deviation, uniaxial compression and fracture performances were systematically studied. More importantly, the effects of maximum strain value on their hyperelastic properties were investigated. Insights in this work will contribute to a better understanding of the manufacturability and hyperelastic properties of the Ni-Ti TPMS lattice structure, and allow the optimization the structural design of the Ni-Ti TPMS lattice structure.

2. Methodology

2.1. Model Design and Preparation

The gyroid lattice structure was modeled by MATLAB, and its governing equation is:

$$\sin(\frac{2\pi}{a} \cdot x)\cos(\frac{2\pi}{a} \cdot y) + \sin(\frac{2\pi}{a} \cdot y)\cos(\frac{2\pi}{a} \cdot z) + \sin(\frac{2\pi}{a} \cdot z)\cos(\frac{2\pi}{a} \cdot x) = t \quad (1)$$

Among them, the parameters $\boldsymbol{a}$ and $\boldsymbol{t}$ control the side length and volume fraction of the gyroid lattice unit cell, respectively. As shown in Figure 1, a 2^3 lattice structure with the cell side of 8 mm and a volume fraction of 5% was designed in this work. The overall size of the lattice structure was 16 mm × 16 mm × 16 mm. In order to facilitate the loading of the surface, plates with a thickness of 1 mm were added to the upper and lower surfaces of the design model, so the overall size of the model was 18 mm × 16 mm × 16 mm.

Ni-Ti powder (atomic ratio 52.5:47.5) was prepared by electrode induction melting gas atomization technology and purchased from Avimetal Powder Metallurgy Technology Co., Ltd. (Beijing, China). The Ni-Ti powder particles had spherical or near-spherical morphologies and normally distributed particle sizes of 20~50 μm. Ni-Ti gyroid lattice samples (six samples) were prepared using BLT-S210 SLM equipment. Table 1 shows the optimized SLM processing parameters. During the whole process, high-purity argon gas was introduced as the protective gas to make the oxygen content less than 0.1%. The substrate was preheated before processing; the preheating temperature was 200 °C. Once

200 °C was reached, preheating was stopped and then the 3D printing process was started. The alternate scanning strategy between layers was adopted. After printing, the samples were allowed to cool naturally to room temperature in an oven, and then the samples were cut from the substrate using a wire electrical discharge machining (EDM) process. As shown in Figure 2, in order to improve the forming quality, the model was rotated 90 degrees to avoid the cantilever structure.

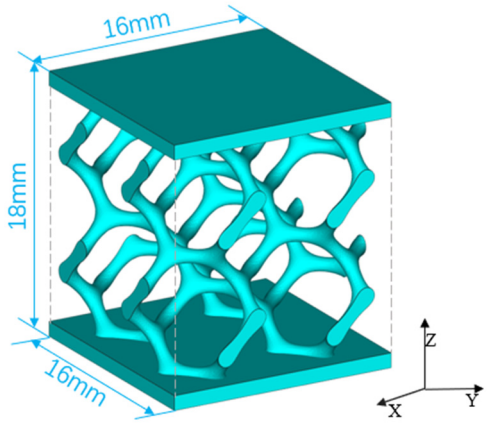

Figure 1. Schematic diagram of the lattice structure model of Ni-Ti lattice structure.

Table 1. SLM parameters of Ni-Ti Gyroid lattice structure.

Laser Power	Scan Speed	Spot Size	Layer Thickness	Scanning Distance
125 W	600 mm/s	50 μm	30 μm	100 μm

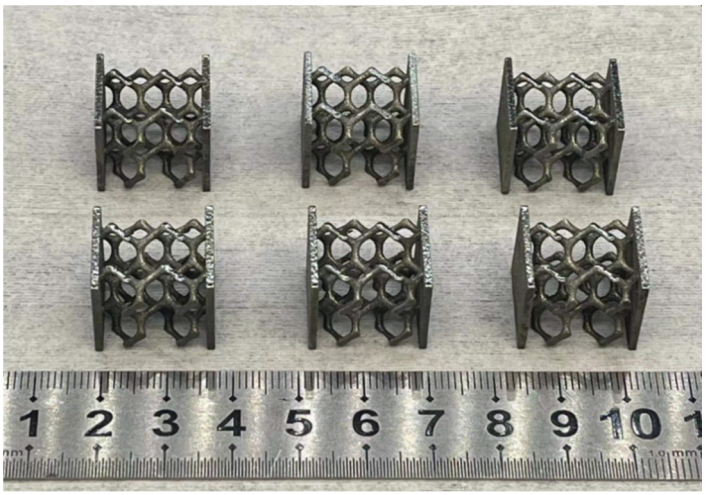

Figure 2. Completed Ni-Ti Gyroid lattice structure.

2.2. Characterization and Testing

The size and weight of SLM samples were measured with SANLIANG micrometer (model 211-101, accuracy 0.001 mm) and METTLER TOLEDO electronic balance (model ME204, accuracy 0.001 g), respectively. The volume of the lattice structure was obtained by the method of absolute ethanol (ethanol content is greater than 99.7%, density is 0.79 g/mL). The density of the model was obtained by dividing the weight by the volume, and then compared with the density of the matrix material (Ni-Ti alloy 6.45 g/cm^3 [34–36]) to determine relative density of the Ni-Ti lattice structure samples. The surface morphology of the SLM samples was observed with a field emission scanning electron microscope (FEI Quanta650 FEG). Uniaxial compression and hyperelasticity tests were performed on Ni-Ti

lattice structures using a SANS CMT5205 electronic universal testing machine from MTS Corporation equipped with a 100 kN load. According to ISO 13314:2011, in the uniaxial compression test, the bottom plate was fixed and the top plate was moved downward at a constant speed, i.e., 0.96 mm/min, to achieve 0.1% strain rate of the entire lattice structure, until the actual travel of the top plate reached the limit stroke or the additional load on the top plate reached the maximum value in the hyperelasticity to the initial position, and then returned to the first step to carry out the secondary compression. A total of 15 cycles was loaded. The testing machine automatically recorded the changes in stroke and load during the compression process and generated data and curves. The compressive stress was obtained by dividing the load value by the effective area of the lattice structure. During the experiment, a high-speed camera was used to capture and record the deformation process of the lattice structure.

The measured size, weight, density and relative density of the gyroid lattice structure samples obtained by additive manufacturing are shown in Table 2. The results showed that the size and weight deviations of the gyroid lattice structure were small (less than 18%), and the relative density of the solid rods of the Ni-Ti Gyroid lattice structure was higher (up to 98.93%), illustrating high manufacturing fidelity.

Table 2. Size, weight, density and relative density of Ni-Ti Gyroid lattice samples.

Sample Number	Experimental Dimensions X × Y × Z	Weight in Air	Weight in Ethanol	Average Density $\overline{\rho^*}$	Average Relative Density η_{RD}
	(mm)	(g)	(g)	(g/cm^3)	(%)
1	18.411 × 15.820 × 16.033	5.4430	4.7696		
2	18.397 × 15.804 × 16.042	5.4272	4.5389	6.381	98.93
3	18.405 × 15.814 × 16.033	5.4504	4.5629		

The actual relative densities and fabrication deviations in Tables 2 and 3 showed that the SLM samples had fabrication deviations higher than the specified value of 15% because of the increased rod diameter and powder adhering to the surface during additive manufacturing [37].This was due to the effects of the heat-affected zone of the molten pool during the SLM process, which transitioned the surrounding powder in a semi-melted state and adhered to the surface of the straight rod. In addition, since the heat dissipation channel of the lattice structure was narrow, the heat accumulation was greater. Furthermore, the specific surface area (surface area to volume ratio) of the lattice structure was larger than that of the bulk material at the same volume. Thus, the increased rod diameter and attached powder had a greater impact on the surface, resulting in a more pronounced fabrication deviation.

Table 3. Manufacturing deviation of Ni-Ti Gyroid lattice structure samples.

Sample Number	Design Weight (g)	Actual Weight (g)	Manufacturing Deviation η_{RD} (%)
1	4.6308	5.4430	17.54
2	4.6308	5.4272	17.20
3	4.6308	5.4504	17.70

Figure 3 shows the SEM surface morphology of the Ni-Ti gyroid lattice structure sample. The additively fabricated lattice structure samples were in good agreement with the designed model, showing circular rods and spherical holes, illustrating that the Ni-Ti gyroid lattice structure could be successfully prepared by SLM technology. In addition, the SLM-fabricated Ni-Ti gyroid lattice appeared rough on many faces due to the adhesion of incompletely melted powder and step effect on the model surface. The reason for this was that, when the laser irradiated the powder support area, the thermal conductivity of

metal powder was lower than that of solid metal, and the absorbed energy could not be fully transmitted to the bottom plate. Thus, more molten powder was prone to sticking under the working layer. Additionally, because the raised profile of the part was usually on the lower outer surface, the lower surface of the part tended to be rougher and more pronounced. Under the direct irradiation of the laser, the upper surface of the part could absorb most of the energy and rarely adhered to the molten powder, so the upper surface of the part appeared smoother.

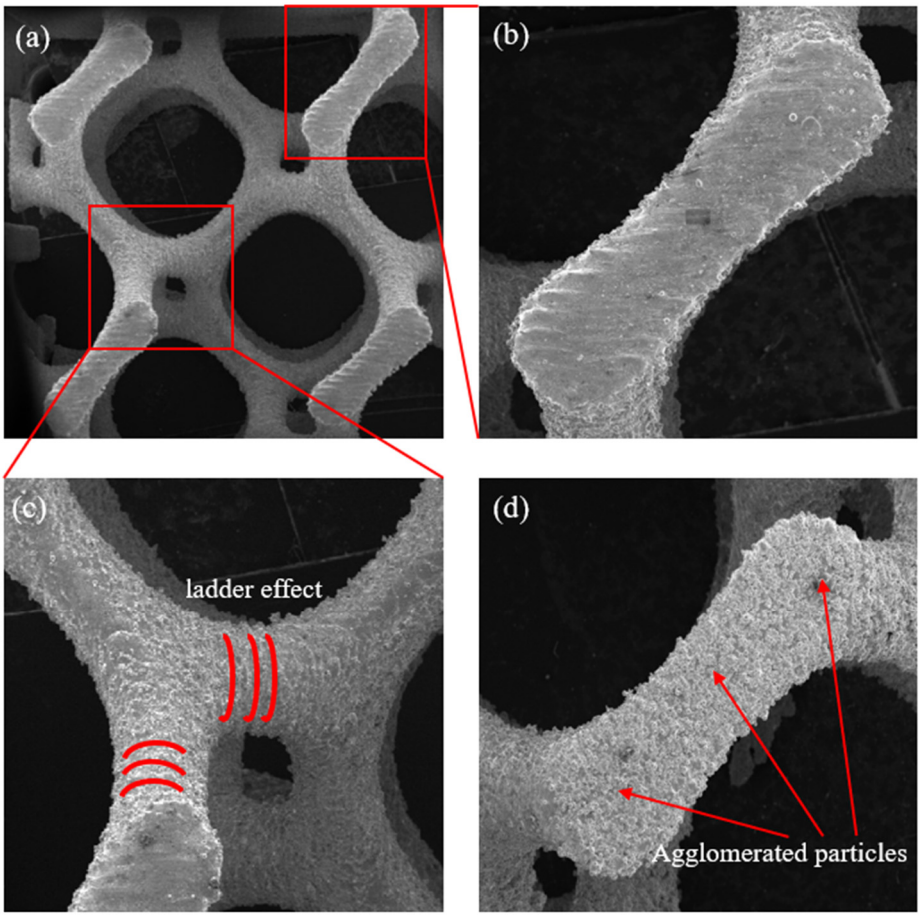

Figure 3. SEM images of the Ni-Ti Gyroid lattice structure prepared by SLM: (**a**–**c**) are the top views of the samples; (**d**) is the bottom views of the samples.

3. Results and Discussion

3.1. Uniaxial Compression Mechanical Properties

As shown in Figure 4, under the uniaxial compression test, the stress–strain curve of the gyroid lattice model experienced an elastic stage and then an elastic-plastic stage before reaching ultimate compressive strength. The stress increased nonlinearly with the increase of strain during the elastic-plastic stage until it reached the maximum stress, representing the ultimate strength. At this time, the total deformation of the model reached about 23%, and no fracture occurred. After a brief yield plateau, the stress–strain curve dropped sharply, marking the fracture of the inner rods of the lattice structure until collapse. It can be observed from Figure 4a–c that as the upper die moved down, the lattice structure underwent significant elastic-plastic deformation, and the deformation was dominated by bending. The first single-bar fractures of gyroid lattice structures occurred on the inclined bars at the corners of these lattice structures with large stress and strain levels. This break occurred first in the bottom layer of the unit cell, and then in the upper layer. It can be seen from the deformation process that almost all the fractures occurred on the inclined rods, while almost none of the horizontal rods were fractured. This was because the fracture

zone was located on the 45° plane of the single-cell inclined rod, and the shear stress there was the largest. The bending deformation of the upper inclined rod caused the surface stress to be concentrated, so the fracture occurred on the inclined rod.

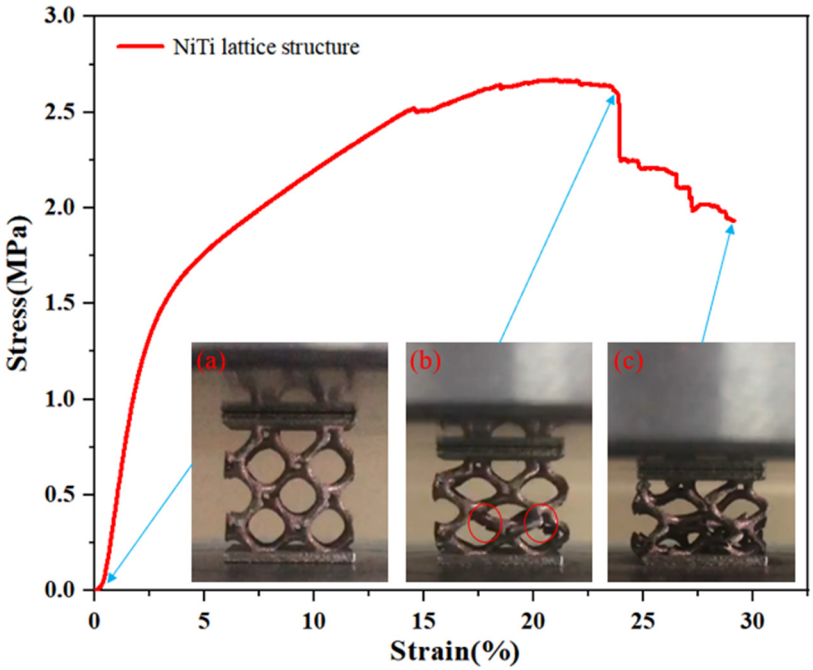

Figure 4. Uniaxial compressive stress–strain curve of the Ni-Ti gyroid lattice structure with the volume fraction of 5%: (**a**–**c**) are the original, initial fracture and collapse stages of the model, respectively.

In the elastic stage of the uniaxial compression experiment, the Poisson's ratio of the Ni-Ti lattice structure was determined by the ratio of the lateral (perpendicular to the pressure direction) strain value and the axial (pressure direction) strain value. Three times were measured. Results showed that the average Poisson's ratio of the lattice structure in the elastic deformation stage was 0.336.

The elastic modulus of a lattice structure can be determined by calculating the slope of the elastic stage of the stress–strain curve in the elastic deformation stage, and the strain value when the strain value deviates from the elastic curve by 0.2% is defined as the yield strength of the model. By fitting the curve, we calculated that the elastic modulus of the Ni-Ti gyroid lattice structure with a volume fraction of 5% was about 130.8 MPa, the yield strength was about 1.2 MPa, the ultimate strength was about 2.7 MPa, and the strain value at the initial fracture was about 24%, indicating that the Ni-Ti gyroid lattice structure fabricated by SLM had good mechanical properties and good toughness.

The experimental results can be used to fit nonlinear equations to predict the mechanical response of gyroid lattice structures with arbitrary volume fractions. The Gibson–Ashby elastic modulus and strength models can be expressed as [38]:

$$\frac{E_{cel}}{E_m} = C_1 \rho^{*m} \tag{2}$$

$$\frac{\sigma_{cel}}{\sigma_m} = C_2 \rho^{*n} \tag{3}$$

$$\rho^* = \frac{\rho_{cel}}{\rho_m} \tag{4}$$

Among them, $\boldsymbol{\rho_m}$, $\boldsymbol{E_m}$, $\boldsymbol{\sigma_m}$ are the density, modulus and strength of the lattice structure substrate, respectively; $\boldsymbol{\rho^*}$ represents the relative density of the lattice structure, that is, the volume fraction; the values of the coefficients $\boldsymbol{C_1}$ and $\boldsymbol{C_2}$ are usually 0.1–4.0 and 0.25–0.35;

m and ***n*** are constants, depending on how the rod is pulled during the deformation of the unit cell: stretching deformation, or bending deformation or a combination of the two [39]. In this article, the value of ***m*** was 2, and the value of ***n*** was 1.5 [40,41].

Through the Gibson–Ashby empirical formula, C_1 = 1.11, C_2 = 0.197 were obtained, and the values were substituted into Formulas (2) and (3). Then, the mechanical responses of the gyroid lattice structures with any volume fraction were predicted. As shown in Figure 5, the gained mechanical properties can be utilized to guide the design of Ni-Ti gyroid lattice structures with specific mechanical properties.

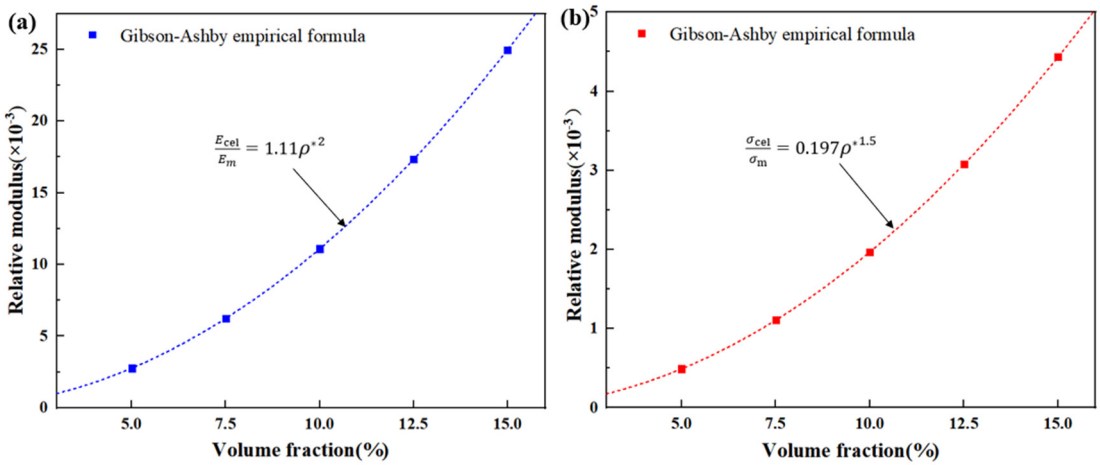

Figure 5. The predicted mechanical properties of Ni-Ti gyroid lattice structures with arbitrary volume fractions: (**a**) relative modulus and (**b**) relative yield strength.

3.2. Hyperelasticity

Hyperelasticity means that, in the process of compression and tension of the alloy, with the loading of stress, the alloy undergoes thermoelastic martensitic transformation and coordinated deformation, and after unloading, reverse transformation occurs to restore the deformation [42]. As shown in Figure 6d, the yield strength, Young's modulus and residual strain in the cyclic compression test are used as parameters to verify the hyperelasticity of the material [43].

Figure 6a–c shows the stress–strain curves and compression process for 15 compression cycles at cyclic strains of 4%, 6%, and 8%. As shown in the figure, the stress–strain curves gradually moved to the right, and the corresponding elastic modulus and residual strain value also changed with the increase of the number of cycles. As shown in Figure 6e, when the maximum strains were 6% and 8%, the elastic modulus was the lowest at the beginning, then rose sharply in the second cycle, and later gradually stabilized with the increase of the number of cycles. The stabilized elastic modulus was about 90 MPa when the maximum strain was 6%, while it was 87 MPa when the strain was 8%. However, when the maximum strain was 4%, the elastic modulus was the largest in the first cycle, reaching 103 MPa, dropped to 95 MPa in the second cycle, and then gradually rose and stabilized around 100 MPa. Comparing the three curves, it was found that with the increase of the maximum strain value, the value of the elastic modulus of the sample gradually decreased; with the increase of the number of cycles, the elastic modulus of each strain value tended to be stable. This can be explained by the residual martensite and work hardening effect. First, some martensite could not be transformed into austenite during the springback process, and the residual martensite would affect Young's modulus of the whole structure [44]. In addition, the work hardening during processing contributed to the change of Young's modulus [45].

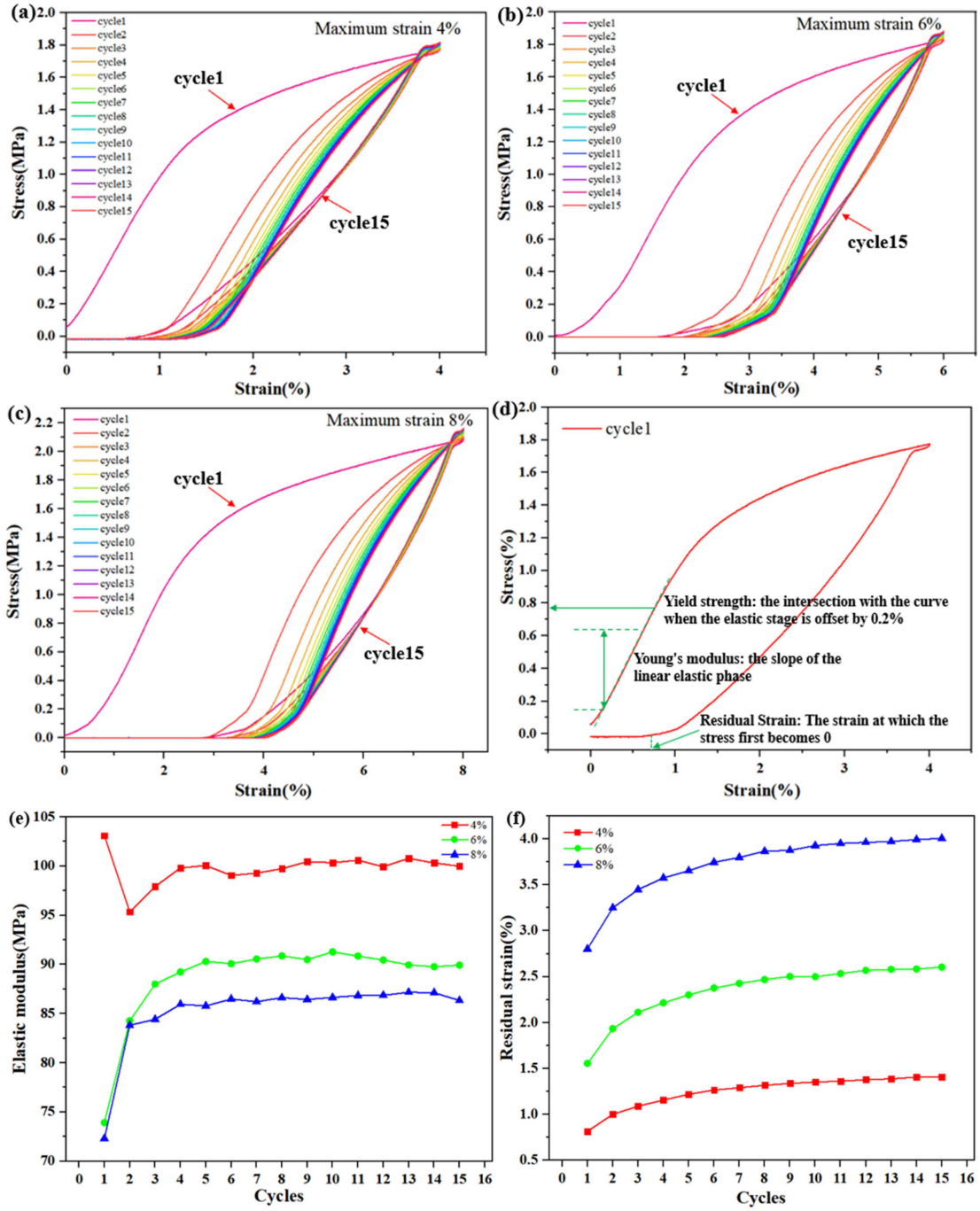

Figure 6. Cyclic compression test curve of Ni-Ti gyroid lattice structure: (**a**–**c**) are the stress–strain curves with maximum strain values of 4%, 6%, and 8%, respectively; (**d**) is the calculation diagram of the elastic modulus and residual strain; (**e**,**f**) are the graphs of the elastic modulus and residual strain with the increase of loading cycles, respectively.

As can be seen from Figure 6f, in the three strain conditions, the residual strain value of the model showed an upward trend with the increase of the number of cycles. When the maximum strain values were 4%, 6%, and 8%, the residual strain increased from 0.8% to 1.4%, from 1.5% to 2.6% and from 2.8% to 4%, respectively. Additionally, with the increase of the maximum strain, the residual strain value also kept increasing. It was noted that, under the action of cyclic loading, the hyperelasticity of the Ni-Ti gyroid lattice structure fabricated by SLM had a functional attenuation, manifested as an increase in residual strain, which was a functional fatigue behavior. At the same time, after a certain cycle

period, the unrecoverable strain of the lattice structure tended to be stable, showing stable hyperelasticity. In addition, with the increase of the cyclic strain value, the unrecoverable strain gradually rose due to the formation of lattice defects in the Ni-Ti material under the action of large strain, which, in turn, hindered the phase transformation of martensite [46].

4. Conclusions

In this paper, a Ni-Ti gyroid-type TPMS lattice structure with a volume fraction of 5% and a cell size of 8 mm was fabricated by SLM. Its manufacturability, compressive mechanical properties, and hyperelastic properties were investigated. The conclusions were as follows:

(1) The relative density of the Ni-Ti gyroid TPMS lattice structure manufactured by SLM was able to reach 98.93%. The average manufacturing deviation of the model was about 17%, showing good manufacturability.

(2) The elastic modulus of the Ni-Ti Gyroid lattice structure was about 130.8 MPa, the yield strength was about 1.2 MPa, the ultimate strength was about 2.7 MPa, and the strain value at the initial fracture was about 24%, indicating that the Ni-Ti gyroid lattice structure fabricated by SLM has good mechanical properties.

(3) In the hyperelasticity test, the elastic modulus and residual strain of the Ni-Ti gyroid TPMS lattice structure gradually became stable with increasing numbers of cycles. When the applied maximum strain increased from 4% to 8%, the elastic modulus decreased from 100 MPa to 87 MPa, and the residual strain increased from 1% to 4%. After a certain cycle period, the hyperelasticity of the lattice structure tended to be stable, showing the stable recoverable strain.

Author Contributions: Conceptualization, C.Z. and L.Y.; methodology, L.Y.; software, J.J.; validation, J.J. and M.H.; formal analysis, C.Z. and L.Y.; investigation, J.J. and M.H.; resources, M.H. and L.Y.; data curation, C.Z. and L.Y.; writing—original draft preparation, J.J.; writing—review and editing, C.Z. and L.Y.; visualization, J.J. and L.Y.; supervision, C.Z. and L.Y.; project administration, C.Z. and L.Y.; funding acquisition, L.Y. All authors have read and agreed to the published version of the manuscript.

Funding: This research was funded by the National Natural Science Foundation of China (No. 52105396), China Postdoctoral Science Foundation (No.2020M6824), Natural Science Foundation of Hubei Province (No. 2021CFB003), and Fundamental Research Funds for the Central Universities (No. 2021IVA053 and 2021III027JC).

Institutional Review Board Statement: Not applicable.

Informed Consent Statement: Not applicable.

Data Availability Statement: Not applicable.

Acknowledgments: Authors would like to thank the National Natural Science Foundation of China (No. 52105396), China Postdoctoral Science Foundation (No.2020M6824), Natural Science Foundation of Hubei Province (No. 2021CFB003), and Fundamental Research Funds for the Central Universities (No. 2021IVA053 and 2021III027JC).

Conflicts of Interest: The authors declare no conflict of interest.

References

1. Wang, X.; Yu, J.; Liu, J.; Chen, L.; Yang, Q.; Wei, H.; Sun, J.; Wang, Z.; Zhang, Z.; Zhao, G.; et al. Effect of process parameters on the phase transformation behavior and tensile properties of NiTi shape memory alloys fabricated by selective laser melting. *Addit. Manuf.* **2020**, *36*, 101545. [CrossRef]
2. Zhao, M.; Qing, H.; Wang, Y.; Liang, J.; Zhao, M.; Geng, Y.; Liang, J.; Lu, B. Superelastic behaviors of additively manufactured porous NiTi shape memory alloys designed with Menger sponge-like fractal structures. *Mater. Des.* **2021**, *200*, 109448. [CrossRef]
3. Costa, M.M.; Bartolomeu, F.; Palmeiro, J.; Guimarães, B.; Alves, N.; Miranda, G.; Silva, F.S. Multi-material NiTi-PEEK hybrid cellular structures by selective laser melting and hot pressing: Tribological characterization. *Tribol. Int.* **2021**, *156*, 106830. [CrossRef]
4. Yu, L.; Chen, K.; Zhang, Y.; Liu, J.; Yang, L.; Shi, Y. Microstructures and mechanical properties of NiTi shape memory alloys fabricated by wire arc additive manufacturing. *J. Alloys Compd.* **2022**, *892*, 162193. [CrossRef]

5. Ibrahim, M.K.; Hamzah, E.; Saud, S.N.; Nazim, E.M. Powder metallurgy fabrication of porous 51 (at.%) Ni-Ti shape memory alloys for biomedical applications. *Shape Mem. Superelast.* **2018**, *4*, 327–336. [CrossRef]
6. Wei, L.; Zhang, X.; Geng, L. Microstructure and properties of NiTi foams with 69% porosity. *Vacuum* **2019**, *162*, 15–19. [CrossRef]
7. Yuan, B.; Zhang, X.P.; Chung, C.; Zhu, M.; Zeng, M.Q. A comparative study of the porous TiNi shape-memory alloys fabricated by three different processes. *Metall. Mater. Trans. A* **2006**, *37*, 755–761. [CrossRef]
8. Köhl, M.; Bram, M.; Moser, A.; Buchkremer, H.; Beck, T.; Stöver, D. Characterization of porous, net-shaped NiTi alloy regarding its damping and energy-absorbing capacity. *Mater. Sci. Eng. A* **2011**, *528*, 2454–2462. [CrossRef]
9. Wang, X.; Xu, S.; Zhou, S.; Xu, W.; Leary, M.; Choong, P.; Qian, M.; Brandt, M.; Xie, Y.M. Topological design and additive manufacturing of porous metals for bone scaffolds and orthopaedic implants: A review. *Biomaterials* **2016**, *83*, 127–141. [CrossRef]
10. Yang, L.; Wu, S.; Yan, C.; Chen, P.; Zhang, L.; Han, C.; Cai, C.; Wen, S.; Zhou, Y.; Shi, Y. Fatigue properties of Ti-6Al-4V Gyroid graded lattice structures fabricated by laser powder bed fusion with lateral loading. *Addit. Manuf.* **2021**, *46*, 102214. [CrossRef]
11. Al-Ketan, O.; Al-Rub, R.K.A. Multifunctional mechanical metamaterials based on triply periodic minimal surface lattices. *Adv. Eng. Mater.* **2019**, *21*, 1900524. [CrossRef]
12. Zhang, S.; Wei, Q.; Cheng, L.; Li, S.; Shi, Y. Effects of scan line spacing on pore characteristics and mechanical properties of porous Ti6Al4V implants fabricated by selective laser melting. *Mater. Des.* **2014**, *63*, 185–193. [CrossRef]
13. Al-Ketan, O.; Rowshan, R.; Abu Al-Rub, R.K. Topology-mechanical property relationship of 3D printed strut, skeletal, and sheet based periodic metallic cellular materials. *Addit. Manuf.* **2018**, *19*, 167–183. [CrossRef]
14. Dong, Y.; Jiang, H.; Chen, A.; Yang, T.; Gao, S.; Liu, S. Near-zero-shrinkage Al2O3 ceramic foams with coral-like and hollow-sphere structures via selective laser sintering and reaction bonding. *J. Eur. Ceram. Soc.* **2021**, *41*, 239–246. [CrossRef]
15. Zhang, X.; Yan, X.; Fang, G.; Liu, M. Biomechanical influence of structural variation strategies on functionally graded scaffolds constructed with triply periodic minimal surface. *Addit. Manuf.* **2020**, *32*, 101015. [CrossRef]
16. Saghaian, S.E.; Amerinatanzi, A.; Moghaddam, N.S.; Majumdar, A.; Nematollahi, M.; Saedi, S.; Elahinia, M.; Karaca, H.E. Mechanical and shape memory properties of triply periodic minimal surface (TPMS) NiTi structures fabricated by selective laser melting. *Biol. Eng. Med.* **2018**, *3*, 1–7.
17. Yang, Q.; Sun, Y.K.; Yang, C.; Sun, M.; Peng, H.; Shen, X.; Huang, S.; Chen, J. Compression and superelasticity behaviors of NiTi porous structures with tiny strut fabricated by selective laser melting. *J. Alloys Compd.* **2021**, *858*, 157674. [CrossRef]
18. Bartolomeu, F.; Costa, M.; Alves, N.; Miranda, G.; Silva, F. Engineering the elastic modulus of NiTi cellular structures fabricated by selective laser melting. *J. Mech. Behav. Biomed. Mater.* **2020**, *110*, 103891. [CrossRef]
19. Yang, L.; Yan, C.; Cao, W.; Liu, Z.; Song, B.; Wen, S.; Zhang, C.; Shi, Y.; Yang, S. Compression–compression fatigue behaviour of gyroid-type triply periodic minimal surface porous structures fabricated by selective laser melting. *Acta Mater.* **2019**, *181*, 49–66. [CrossRef]
20. Zhang, C.; Zheng, H.; Yang, L.; Li, Y.; Jin, J.; Cao, W.; Yan, C.; Shi, Y. Mechanical responses of sheet-based gyroid-type triply periodic minimal surface lattice structures fabricated using selective laser melting. *Mater. Des.* **2022**, *214*, 110407. [CrossRef]
21. Saedi, S.; Saghaian, S.E.; Jahadakbar, A.; Moghaddam, N.S.; Andani, M.T.; Lu, Y.C.; Elahinia, M.; Karaca, H.E. Shape memory response of porous NiTi shape memory alloys fabricated by selective laser melting. *J. Mater. Sci. Mater. Med.* **2018**, *29*, 40. [CrossRef] [PubMed]
22. Ibrahim, H.; Jahadakbar, A.; Dehghan, A.; Moghaddam, N.S.; Amerinatanzi, A.; Elahinia, M. In Vitro Corrosion Assessment of Additively Manufactured Porous NiTi Structures for Bone Fixation Applications. *Metals* **2018**, *8*, 164. [CrossRef]
23. Ashrafi, M.J.; Amerinatanzi, A.; Saebi, Z.; Moghaddam, N.S.; Mehrabi, R.; Karaca, H.; Elahinia, M. Shape memory response of cellular latticestructures: Unit cell finite element prediction. *Mech. Mater.* **2018**, *125*, 26–34. [CrossRef]
24. Andani, M.T.; Saedi, S.; Turabi, A.S.; Karamooz, M.R.; Haberland, C.; Karaca, H.E.; Elahinia, M. Mechanical and shape memory properties of porous Ni50.1Ti49.9 alloys manufactured by selective laser melting. *J. Mech. Behav. Biomed. Mater.* **2017**, *68*, 224–231. [CrossRef] [PubMed]
25. Ravari, M.R.K.; Esfahani, S.N.; Andani, M.T.; Kadkhodaei, M.; Ghaei, A.; Karaca, E.H.; Elahinia, M. On the effects of geometry, defects, and material asymmetry on the mechanical response of shape memory alloy cellular lattice structures. *Smart Mater. Struct.* **2016**, *25*, 025008. [CrossRef]
26. Dadbakhsh, S.; Speirs, M.; Kruth, J.-P.; Van Humbeeck, J. Influence of SLM on shape memory and compression behaviour of NiTi scaffolds. *CIRP Ann. Manufact. Technol.* **2015**, *64*, 209–212. [CrossRef]
27. Habijan, T.; Haberland, C.; Meier, H.; Frenzel, J.; Wittsiepe, J.; Wuwer, C.; Greulich, C.; Schildhauer, T.; Köller, M. The biocompatibility of dense and porous Nickel–Titanium produced by selective laser melting. *Mater. Sci. Eng. C* **2013**, *33*, 419–426. [CrossRef]
28. Yang, L.; Mertens, R.; Ferrucci, M.; Yan, C.; Shi, Y.; Yang, S. Continuous graded Gyroid cellular structures fabricated by selective laser melting: Design, manufacturing and mechanical properties. *Mater. Des.* **2019**, *162*, 394–404. [CrossRef]
29. Al-Saedi, D.S.J.; Masood, S.H.; Faizan-Ur-Rab, M.; Alomarah, A.; Ponnusamy, P. Mechanical properties and energy absorption capability of functionally graded F2BCC lattice fabricated by SLM. *Mater. Des.* **2018**, *144*, 32–44. [CrossRef]
30. Mazur, M.; Leary, M.; Sun, S.; Vcelka, M.; Shidid, D.; Brandt, M. Deformation and failure behaviour of Ti-6Al-4V lattice structures manufactured by selective laser melting (SLM). *Int. J. Adv. Manufact. Technol.* **2015**, *84*, 1391–1411. [CrossRef]

31. Yang, E.; Leary, M.; Lozanovski, B.; Downing, D.; Mazur, M.; Sarker, A.; Khorasani, A.; Jones, A.; Maconachie, T.; Bateman, S.; et al. Effect of geometry on the mechanical properties of Ti-6Al-4V Gyroid structures fabricated via SLM: A numerical study. *Mater. Des.* **2019**, *184*, 108165. [CrossRef]
32. Yang, L.; Yan, C.; Han, C.; Chen, P.; Yang, S.; Shi, Y. Mechanical response of a triply periodic minimal surface cellular structures manufactured by selective laser melting. *Int. J. Mech. Sci.* **2018**, *148*, 149–157. [CrossRef]
33. Speirs, M.; Van Hooreweder, B.; Van Humbeeck, J.; Kruth, J.-P. Fatigue behaviour of NiTi shape memory alloy scaffolds produced by SLM, a unit cell design comparison. *J. Mech. Behav. Biomed. Mater.* **2017**, *70*, 53–59. [CrossRef] [PubMed]
34. Zhan, J.-B.; Lu, Y.-J.; Lin, J.-X. On the Martensitic Transformation Temperatures and Mechanical Properties of NiTi Alloy Manufactured by Selective Laser Melting: Effect of Remelting. *Acta Metall. Sin.* **2021**, *34*, 1223–1233. [CrossRef]
35. Vieira de Oliveira, R.; Pereira de Lima, Y.; Hoisler Sallet, E.; Abílio Corrêa Gonçalves, D.; Vieira Le Sénèchal, N.; Alves Oliveira Melo, E.; Rodrigues, P.F.; Neto, P.I.; da Silva, J.V.L.; dos Santos Paula, A.; et al. Production of Cylindrical Specimens Based on the Ni-Ti System by Selective Laser Melting from Elementary Powders. *J. Mater. Eng. Perform.* **2021**, *30*, 5477–5490. [CrossRef]
36. Qin, S.; Zhan, J.; Lu, Y.; Lin, J. Effect of energy input on the density and shape memory effect of NiTi alloy by selective laser melting in different hatch spacing. *Mater. Technol.* **2021**, 1–13. [CrossRef]
37. Yang, L.; Ferrucci, M.; Mertens, R.; Dewulf, W.; Yan, C.; Shi, Y.; Yang, S. An investigation into the effect of gradients on the manufacturing fidelity of triply periodic minimal surface structures with graded density fabricated by selective laser melting. *J. Mater. Process. Technol.* **2020**, *275*, 116367. [CrossRef]
38. Gibson, L.J. Mechanical Behavior of Metallic Foams. *Annu. Rev. Mater. Sci.* **2000**, *30*, 191–227. [CrossRef]
39. Maskery, I.; Aremu, A.O.; Simonelli, M.; Tuck, C.; Wildman, R.; Ashcroft, I.; Hague, R. Mechanical Properties of Ti-6Al-4V Selectively Laser Melted Parts with Body-Centred-Cubic Lattices of Varying cell size. *Exp. Mech.* **2015**, *55*, 1261–1272. [CrossRef]
40. Gibson, L.; Ashby, M. *Cellular Solids: Structure and Properties*; Cambridge University Press: Cambridge, NY, USA, 1997; pp. 444–449.
41. Li, Q.M.; Magkiriadis, I.; Harrigan, J.J. Compressive Strain at the Onset of Densification of Cellular Solids. *J. Cell. Plast.* **2016**, *42*, 371–392. [CrossRef]
42. Wang, Q.; He, Z.; Wang, F.; Liu, Y.; Yang, J. Research Progress of Superelasticity in Ti-Ni Shape Memory Alloy. *Mater. Rev.* **2010**, *24*, 85–88.
43. Omori, T.; Iwaizako, H.; Kainuma, R. Abnormal grain growth induced by cyclic heat treatment in Fe-Mn-Al-Ni superelastic alloy. *Mater. Des.* **2016**, *101*, 263–269. [CrossRef]
44. Šittner, P.; Heller, L.; Pilch, J.; Curfs, C.; Alonso, T.; Favier, D. Young's Modulus of Austenite and Martensite Phases in Superelastic NiTi Wires. *J. Mater. Eng. Perform.* **2014**, *23*, 2303–2314. [CrossRef]
45. Shi, Y.D.; Wang, L.N.; Liang, S.X.; Zhou, Q.; Zheng, B. A high Zr-containing Ti-based alloy with ultralow Young's modulus and ultrahigh strength and elastic admissible strain. *Mater. Sci. Eng. A* **2016**, *674*, 696–700. [CrossRef]
46. Ye, J.J.; He, Z.R.; Zhang, K.G.; Du, Y.Q. Research Progress of Effect of Heat Treatment on Microstructure, Phase Transformation Behaviors and Memory Properties in Ti-Ni Based Shape Memory Alloys. *Mater. Sci. Forum* **2021**, *6187*, 20–31. [CrossRef]